

Document downloaded from:

<http://hdl.handle.net/10251/143118>

This paper must be cited as:

Hernández-Montoto, A.; Montes-Robles, R.; Samadi, A.; Gorbe, M.; Terrés-Haro, JM.; Cao Milán, R.; Aznar, E.... (08-2). Gold Nanostars Coated with Mesoporous Silica Are Effective and Nontoxic Photothermal Agents Capable of Gate Keeping and Laser Induced Drug Release. ACS Applied Materials & Interfaces. 10(33):27644-27656.  
<https://doi.org/10.1021/acsami.8b08395>



The final publication is available at

<https://doi.org/10.1021/acsami.8b08395>

Copyright American Chemical Society

Additional Information

# Gold Nanostars Coated with Mesoporous Silica are Effective and Non-Toxic Photothermal Agents Capable of Gate Keeping and Laser Induced Drug Release

*Andy Hernández Montoto,<sup>‡</sup> Roberto Montes,<sup>‡</sup> Akbar Samadi,<sup>Γ</sup> Mónica Gorbe,<sup>‡, 1</sup> José Manuel Terrés,<sup>‡</sup> Roberto Cao-Milán,<sup>||</sup> Elena Aznar,<sup>‡, 1, 1, 1</sup> Javier Ibañez,<sup>‡</sup> Rafael Masot,<sup>‡</sup> María Dolores Marcos,<sup>‡, 1, 1, 1, 1</sup> Mar Orzáez,<sup>1</sup> Félix Sancenón,<sup>‡, 1, 1, 1</sup> Lene B. Oddershede<sup>\*, Γ</sup> and Ramón Martínez-Mañez<sup>\*, ‡, 1, 1, 1</sup>*

<sup>‡</sup> Instituto Interuniversitario de Investigación de Reconocimiento Molecular y Desarrollo Tecnológico (IDM). Universitat Politècnica de Valencia, Universitat de València, Camino de Vera s/n, 46022 Valencia, Spain

<sup>||</sup> CIBER de Bioingeniería, Biomateriales y Nanomedicina (CIBER-BBN)

<sup>1</sup> Departamento de Química, Universitat Politècnica de València, Camino de Vera s/n, 46022 Valencia, Spain

J Unidad Mixta UPV-CIPF de Investigación en Mecanismos de Enfermedades y Nanomedicina, Valencia, Universitat Politècnica de València, Centro de Investigación Príncipe Felipe, València, Spain.

Γ Niels Bohr Institute, University of Copenhagen, 2100 Copenhagen, Denmark.

И Facultad de Química, Universidad de La Habana, 10400 La Habana, Cuba.

KEYWORDS: gold nanostars, mesoporous silica shell, thermo-sensitive molecular gates, optical heating, drug photo-release

#### ABSTRACT

Herein, a novel drug photo-release system based on gold nanostars (AuNSts) coated with a mesoporous silica shell and capped with paraffin as thermo-sensitive molecular gate, is reported. Direct measurements of the surface temperature of a single gold nanostar irradiated by a tightly focused laser beam, are performed via a heat-sensitive biological matrix. The surface temperature of an AuNSt increases by hundreds of degrees Celsius even at low laser powers. AuNSts coated with a mesoporous silica shell using a surfactant-templated synthesis are used as chemotherapeutic nanocarriers. Synthetic parameters are optimized to avoid AuNSts reshaping, thus to obtain nanoparticles with suitable and stable plasmonic properties for near-infrared (NIR) laser triggered cargo delivery. The mesoporous silica coated nanostars are loaded with doxorubicin (Dox) and coated with octadecyltrimethoxysilane and the paraffin heneicosane. The paraffin molecules set up a hydrophobic layer that blocks the pores, impeding the release of the cargo. This hybrid nanosystem exhibits a well-defined photo-delivery profile using NIR

radiations, even at low power density, whereas the non-irradiated sample shows a negligible payload release. Dox loaded nanoparticles displayed no cytotoxicity toward HeLa cells, until they are irradiated with 808 nm laser, provoking paraffin melting and drug release. Hence, these novel, functional and bio-compatible nanoparticles display adequate plasmonic properties for NIR triggered drug photo-release applications.

## INTRODUCTION

Drug release systems remotely controlled by near-infrared (NIR) light irradiation have received increasing attention in cancer therapy because cargo release can be defined spatially and temporally by fine-tuning the area and time of the light stimulus.<sup>1-2</sup> Moreover, the use of NIR radiation (700–1100 nm) is especially appealing for biological applications due to its deeper tissue penetration and minimal damage to healthy tissues.<sup>3</sup> Currently, studies have been focused on finding different ways to create complex systems based on nanoparticles which can simultaneously store drugs efficiently and activate a mechanism for its delivery using NIR light irradiation.<sup>4-6</sup>

Because of their pronounced localized surface plasmon resonance (LSPR), anisotropic gold nanoparticles efficiently absorb NIR radiation and convert it to thermal energy.<sup>7-9</sup> Among anisotropic gold nanoparticles, AuNSts, with multiple sharp branches, have superior light-to-heat conversion efficiency<sup>10-12</sup> due to the strong electromagnetic field enhancement taking place at their sharp tips, acting as multiple hot spots.<sup>13-14</sup> In order to evaluate and compare the heating efficiency of individual nanoparticles and thereby their potential for cancer therapy applications (such as hyperthermia and photothermal triggered drug delivery), it is crucial to know the exact temperature profile around a single irradiated nanoparticle. For direct quantification of the

temperature profile of an irradiated nanoparticle, one can use a biological matrix with a well-defined phase transition temperature as sensor as demonstrated for various types of nanoparticles,<sup>15-17</sup> however, not yet for AuNSts.

On the other hand, mesoporous silica (MS) supports are especially appealing as drug nanocarriers because of their unique properties, such as chemical stability, high loading capacity, low cost, and biocompatibility. MS can be prepared in different forms ranging from micrometric to nanometric and have tailor-made pores (2–10 nm in diameter) and large specific surface areas (up to 1200 m<sup>2</sup> g<sup>-1</sup>) and volumes. Moreover, MS can be functionalized with (bio)chemical or supramolecular ensembles than act as “molecular gates” for the development of stimuli-responsive systems able to release an entrapped cargo in the presence of certain and well-defined stimuli.<sup>1</sup>

There are few photo-delivery systems reported in the literature that combine plasmonic gold nanoparticles and gated mesoporous materials.<sup>1</sup> These reported systems are based on gold nanorods<sup>18-23</sup> or nanocages<sup>24</sup> coated with a mesoporous silica shell and capped with thermo-sensible gatekeepers, such as smart polymers,<sup>19, 24</sup> phase changing materials,<sup>18</sup> oligonucleotides<sup>20-22</sup> and supramolecular switches.<sup>23</sup> However, AuNSts coated with gated mesoporous silica shell have not yet been employed for NIR laser triggered photo-release applications in spite of their superior plasmonic properties,<sup>10-12</sup> and their use in intracellular imaging<sup>25-26</sup> and photo-thermal therapy applications.<sup>27-28</sup>

We report herein an optimization of the synthesis of AuNSts coated with a mesoporous silica shell (AuNSt@mSiO<sub>2</sub>). Also, we quantify the heating and drug release capabilities of the MS-coated AuNSts relevant for controlled release applications using NIR irradiation. To this end, AuNSt@mSiO<sub>2</sub> nanoparticles were loaded with Dox and capped with the paraffin heneicosane

(AuNSt@mSiO<sub>2</sub>@Dox@paraffin). We found that un-irradiated AuNSt@mSiO<sub>2</sub>@Dox@paraffin nanoparticles remained capped with a negligible leak of cargo. Irradiation with 808 nm light produces a temperature increase in the surroundings of the AuNSts, melting of the gating paraffin, and induces the cargo release. Dox loaded nanoparticles shows no cytotoxicity toward HeLa cells until they are irradiated with 808 nm laser, corroborating the gating efficiency of paraffin and the activation mechanism of drug release due to the photothermal conversion by AuNSts. Also, using a biological matrix we quantified the temperature profile around NIR irradiated single bare or polymer (PVP) coated AuNSt. The heating associated with NIR irradiation of AuNSts is dependent on laser power and on whether or not the AuNSt is coated with the polymer. Both with and without coating temperatures up to 100 Celsius, more than sufficient for cancer treatment, could be reached at relatively low laser powers (less than 50 mW).

## EXPERIMENTAL SECTION

**Chemicals.** Tetrachloroauric acid aqueous solution 30%, sodium citrate trihydrate, polyvinylpyrrolidone (PVP,  $M_w=10000$ ), *N,N*-dimethylformamide (DMF), hexadecyltrimethylammonium bromide (CTAB), tetraethoxysilane, ammonia aqueous solution 32%, ammonium nitrate, octadecyltrimethoxysilane and heneicosane were purchased from Aldrich. Doxorubicin hydrochloride was purchased from Carbosynth Limited. Analytical grade solvents were purchased from Scharlau. HeLa cells were purchased from the German Resource Center for Biological Materials. Dulbecco's Modified Eagle Medium (DMEM), Fetal Bovine Serum (FBS), Dulbecco's Phosphate Buffer Saline (PBS), trypsin, Hoechst 33342 and cell proliferation reagent WST-1 were purchased from Sigma-Aldrich.

**Instrumentation.** Transmission electron microscopy (TEM) images were collected using a JEOL JEM-1010 microscope operating at 100 kV. Dark-field scanning transmission electron microscopy (HAADF-STEM) images, energy dispersive X-ray spectroscopy (EDXS) and energy dispersive X-ray spectroscopy element mapping were performed on JEOL JEM-2100F microscope operating at 200 kV. Field-emission scanning electron microscopy (FE-SEM) images were obtained on a ZEISS ULTRA55 microscope. Optical extinction spectra were recorded using a JASCO V-650 UV/vis spectrophotometer. Fluorescence spectroscopy was carried out on a JASCO FP-8300 spectrofluorometer (Hitachi High Technologies). Fourier transform infrared (FT-IR) spectra were recorded using a Bruker TENSOR27 spectrometer. X-ray measurements were performed on a Bruker AXS D8 Advance diffractometer using Cu-K $\alpha$  radiation. Thermo-gravimetric analyses were carried out on a TGA/SDTA 851e Mettler Toledo equipment, using an oxidant atmosphere (Air, 80 ml min<sup>-1</sup>) with a heating program consisting on a heating step from 298 K to 373 K at heating rate of 10 °C per minute, then an isothermal heating step at 373 K during 30 minutes, a third heating step from 373 K to 1273 K at heating rate of 10 °C per minute and finally an isothermal heating step at 1273 K during 30 minutes. N<sub>2</sub> adsorption-desorption isotherms were recorded on a Micromeritics ASAP2010 automated sorption analyzer. The samples were degassed at 120 °C under vacuum overnight. The specific surface areas were calculated from the adsorption data in the low pressures range using the Brunauer-Emmett-Teller (BET) method. Pore size was determined by following the Barrett–Joyner–Halenda (BJH) model. Hydrodynamic diameter and zeta potential measurements were performed by dynamic light scattering using a Malvern Zeta sizer Nano ZS instrument.

**Synthesis of 15 nm and 40 nm gold nanospheres seeds.** Citrate coated gold nanoparticles with the diameter of 15 and 40 nm were obtained by Turkevich-Frens method<sup>29-31</sup> and Bastús

protocol,<sup>32</sup> respectively. Both nanoparticle samples were coated with PVP according to procedure reported by Graf et al.<sup>33</sup> The concentration of Au in all colloids was obtained from their extinction spectra (absorbance at 400 nm).<sup>34-35</sup>

**Synthesis of bare gold nanostars (AuNSt).** AuNSts were synthesized by seeded growth method using PVP solution in DMF with minor modification.<sup>36-38</sup> At 25°C, an aqueous solution of HAuCl<sub>4</sub> (750 µL; 166 mM) was mixed with a PVP solution in DMF (150 mL; 10 mM). After 5 min, a preformed seed dispersion (100 µL; 15 nm gold nanospheres coated with PVP in ethanol, c(Au) = 6.5 mM) was added and allowed to react for 24 h without stirring. Gold nanoparticles were recovered by centrifugation (20 min; 9500 rpm) and washed five times with water by centrifugation and redispersion. Nanoparticle concentration in AuNSt sample was calculated using the number of Au atoms per particle that can be estimated assuming AuNSt have quasi-spherical morphology in order to determine nanoparticle volume from TEM images. The detailed calculation procedure of nanoparticle concentration in AuNSt is included in the Supporting Information.

**Synthesis of PVP-coated AuNSt (AuNSt@PVP).** AuNSts were synthesized by seeded growth method using PVP solution in DMF with minor modification.<sup>36-38</sup> At 25 °C, an aqueous solution of HAuCl<sub>4</sub> (750 µL; 166 mM) was mixed with a PVP solution in DMF (150 mL; 10 mM). After 5 min, a preformed seed dispersion (100 µL; 40 nm Au nanospheres coated with PVP in ethanol, c(Au) = 8.5 mM) was added and allowed to react for 24 h without stirring. Au nanoparticles were recovered by centrifugation (20 min; 9500 rpm) and washed one time with water by centrifugation and redispersion.

**Synthesis of mesoporous silica shell-coated AuNSt (AuNSt@mSiO<sub>2</sub>).** At 25 °C, a CTAB aqueous solution (50 mL; 6.6 mM) was mixed with ethanol (20 mL) in a round bottom flask (250

mL) under magnetic stirring (400 rpm). Ar gas was bubbled into solution for 1 h and then inert atmosphere was kept until the reaction was completed. Once the solution was free of Ar bubbles, an ammonia aqueous solution (50  $\mu$ L; 32%) was added. Subsequently; a bare AuNSt dispersion (3 mL;  $c(\text{Au}) = 5 \text{ mM}$ ) was poured into the synthesis solution. After 5 min, a predetermined volume of TEOS (30-40  $\mu$ L) was added dropwise. TEOS amount in the reaction mixture was varied in order to obtain the desired nanoparticle size. After 24 hours the particles were recovered (10 min, 9500 rpm) and washed twice in ethanol. Finally, the CTAB template was removed by extraction process dispersing nanoparticles in a  $\text{NH}_4\text{NO}_3$  solution in ethanol (50 mL; 10 mg  $\text{mL}^{-1}$ ). The mixture was stirred for 8 hours and particles were recovered by centrifugation. This extraction process was repeated three times in order to achieve the removal of higher amount of CTAB from mesoporous channels.

**Cargo loading.** The loading of Dox within the mesopores of AuNSt@mSiO<sub>2</sub> nanoparticles and its subsequent functionalization with octadecyl chains was performed following a procedure previously reported by our group with minor modification.<sup>39</sup> Briefly, AuNSt@mSiO<sub>2</sub> nanoparticles (2 mg) was dispersed in ethanol (2 mL). Subsequently, doxorubicin hydrochloride (1 mg) and octadecyltrimethoxysilane (20  $\mu$ L) were added. The mixture was stirred for 12 h at 25 °C. The nanoparticles were recovered by centrifugation and dried under vacuum. Then, Dox loaded nanoparticles were dispersed in *n*-hexane (10 mL) and a heneicosane solution in *n*-hexane (1 mL; 20 mg  $\text{mL}^{-1}$ ) was added. The mixture was dispersed for short periods (1 min) during 30 min using ultrasonic bath and the nanoparticles were recovered by centrifugation and dried under vacuum. The overall fraction of organic materials was estimated by TGA measurements. The amount of loaded Dox was determined spectrophotometrically by dispersing AuNSt@mSiO<sub>2</sub>@Dox@paraffin nanoparticles (1 mg) in water (1 mL). Then, nanoparticle

suspension was stirred at 60 °C for 48 h in order to extract and transfer Dox into the water. Finally, after centrifugation of nanoparticles, the absorbance at 480 nm of supernatant was used to determine the amount of Dox employing a predetermined calibration curve. The detailed calculation procedure of Dox content in nanoparticles is included in the Supporting Information.

**Cargo photo-release.** Before cargo photo-release experiment was performed, AuNSt@mSiO<sub>2</sub>@Dox@paraffin nanoparticles were washed several times with water by centrifugation and redispersion. The NIR laser-triggered drug release experiments were performed with a laser diode (808 nm)<sup>40</sup> that was set at 1 cm above the liquid surface. A well in the 96-well plate was filled with nanoparticles suspensions (250 μL; 100 μg mL<sup>-1</sup>). In this way 30 % of the total sample volume was irradiated at a predetermined power density (0.4 and 4 W cm<sup>-2</sup>). This well and another containing a control sample were placed in an air chamber at 37 °C. At a predetermined interval upon NIR irradiation, the samples were centrifuged (3 min, 9500 rpm) and the released cargo from supernatant was determined through the measurement of the fluorescence emission of Dox at 555 nm ( $\lambda_{\text{exc}} = 488$  nm). Temperature changes of control and irradiated samples were monitored using a fiber-optic thermosensor.

**Cell viability assays.** HeLa cells were grown at 37 °C under humidified air containing CO<sub>2</sub> (5 vol.%) in Dulbecco's Modified Eagle Medium (DMEM), which was supplemented with fetal bovine serum (10 vol.% FBS, Gibco), penicillin/streptomycin (1 vol.% ;10000 units of both per mL). After 24 h of incubation, cells were rinsed with PBS, and then detached with trypsin (0.2 vol.%) /PBS. The HeLa cells were seeded in 96-well plates with a density of 5·10<sup>3</sup> cells per well and grown in DMEM for another 24 h. The cells were then treated with the nanoparticle suspensions in DMEM at different concentrations. Then the designated cells were exposed to a NIR laser irradiation (808 nm, 1 to 4 W cm<sup>-2</sup>, 10-15 min). Upon the switching-off of the laser,

the treated cells were incubated for another 24 or 48 h. After a predetermined incubation period, the cells were rinsed with PBS, and the cell viabilities were evaluated via the WST-1 assay. Typically, cell proliferation reagent WST-1 (7  $\mu\text{L}$ ) was added, and then the cells were incubated for another 1 h at 37  $^{\circ}\text{C}$ . The absorbance at 450 nm was measured using a micro-plate reader (Perkin Elmer Wallac 1420 Victor2). Percentage of cell viabilities were determined relative to the untreated cells (control, 100 % viability). Three replicates were done for each treatment groups.

For NIR light triggered delivery of Dox experiments using confocal laser scanning microscopy (CLSM), cells were seeded over glass coverslips in 6-well plate with a density of  $5 \cdot 10^5$  cells per well and grown in DMEM for 24 h. Cells were incubated with AuNSt@mSiO<sub>2</sub>@Dox@paraffin nanoparticles at 10 and 50  $\mu\text{g mL}^{-1}$  for 2 h. Then, the designated cells were irradiated with 808 nm laser at 4  $\text{W cm}^{-2}$  for 10 min and were incubated for another 2 h. Then, cells were rinsed with PBS, and freshly DMEM was added. Finally, DNA marker Hoechst 33342 (2  $\mu\text{g mL}^{-1}$ ) was added, and cells were incubated for 5 min before CLSM analysis. CLSM image were recorded using a Leica TCS SP8 (Leica Microsystems CMS GmbH) confocal laser scanning microscope.

Cell internalization of nanoparticles was tested by TEM. TEM images were acquired using a microscope FEI Tecnai Spirit G2 operating at 80 kV with a digital camera (Soft Image System, Morada). Hela cells were incubated with nanoparticle suspension in DMEM at 30  $\mu\text{g mL}^{-1}$  for 24 h. Then, cells were fixed with glutaraldehyde (3 %) in sodium phosphate buffer (0.1  $\text{mol L}^{-1}$ ), dehydrated in ethanol and stained with osmium tetroxide (1 %) and uranyl acetate (1 %). Finally, the samples were embedded in epoxy resin (Araldite) and sectioned for analysis.

**Direct measurements of the temperature surrounding single AuNSt.** Direct measurements of the temperature surrounding single irradiated AuNSt were carried out following a protocol

described by Bendix et al.<sup>15</sup> For the lipid bilayer assay where fluorophores partitioned in the gel phase we used 1,2-dipentadecanoyl-*sn*-glycero-3-phosphocholine (DC<sub>15</sub>PC, Avanti Polar lipids) with 3,3'-dilinoleyloxycarbocyanine perchlorate (0.75 mol % DiOC<sub>18:2</sub>) fluorophores (The fluorophores were excited at 488 nm and imaged in the spectral range of 496–587 nm).<sup>16</sup> Lipids suspended in chloroform were dried on glass under nitrogen flow and further dried in vacuum for 2 h. The lipid film was hydrated in PBS buffer at 37 °C. To form small unilamellar vesicles, we extruded the hydrated lipid mass through 50 nm filters at 37 °C. Small unilamellar vesicles were allowed to fuse to a hydrophilic glass surface for 3 h at 37 °C above the gel-to-fluid phase transition. Subsequently, the surfaces were thoroughly washed using Milli-Q water with the surface and fluid held at 37 °C. Nanoparticles suspended in Milli-Q water were added and allowed to adhere to the bilayer. Only nanoparticles that were stuck to the bilayer were used for experiments. Glass surfaces were etched in piranha solution (3:1 sulfuric acid and hydrogen peroxide) for 30 min.

The laser employed for quantifying the temperature profile of irradiated AuNSts was an Nd:YVO<sub>4</sub> (5 W Spectra Physics Millennia  $\lambda=1064$  nm, TEM00) laser coupled into the back port of a Leica confocal laser scanning microscope (SP5/TCS). The laser was focused through a high numerical aperture oil immersion objective (HC, PL, APO, 63.X, NA=1.20 WATER). To improve trapping, the collimated beam slightly overfilled the back aperture of the objective. The position of the focus was accurately positioned, with nanometer precision, relative to the surface using a three-dimensional piezoelectric stage (PI 731.20, Physik Instrumente, Germany). The laser focus was displaced in the axial direction from the optical focus of the microscope to simulate the configuration while trapping a gold nanoparticle in solution. The nanoparticles were imaged in reflection mode (excited by  $\lambda = 594$  nm). Scattered light from the particle and

fluorescent light from the bilayer were collected simultaneously using two photomultiplier tubes. The chambers were heated using a custom-built stage with water circulating from a temperature-controlled water bath with a temperature stability of approximately 0.5 °C. The laser power reaching the objective was measured using a power meter and the transmission through the objective was measured with the dual objective method. The spot size in the plane of the lipid bilayer was measured to be  $d_{spot} = 1.95 \mu\text{m}$  by bleaching an area on a fluorescently labeled gel phase bilayer cooled to 13 °C below the phase transition temperature. We used the maximum output to bleach the molecules in the focal region. The frozen bilayer exhibits very slow diffusion of fluorophores, and hence the bleached area represents the approximate extent of the  $4 \cdot \frac{P}{I} \cdot \frac{1}{2}$ , where  $P$  is the total power delivered at the sample.

## RESULTS AND DISCUSSION

Although the use of AuNSts coated with gated mesoporous silica shell is an interesting and novel approach for NIR laser triggered drug delivery applications, the preparation of these nanodevices can be challenging due to reshaping or partial oxidation the tips of AuNSts with corresponding loss of their optical properties.<sup>36,41-42</sup> For this reason, a tight control of each synthetic step (Figure 1) is necessary to obtain nanoparticles with a homogeneous silica shell and mesopores, and suitable plasmonic properties. Several synthetic conditions including surfactant/TEOS ratio, temperature, inert atmosphere, etc. were tested in order to finally prepare AuNSt@mSiO<sub>2</sub> nanoparticles with minimum changes in the shape and absorption properties of the AuNSt core (*vide infra*).

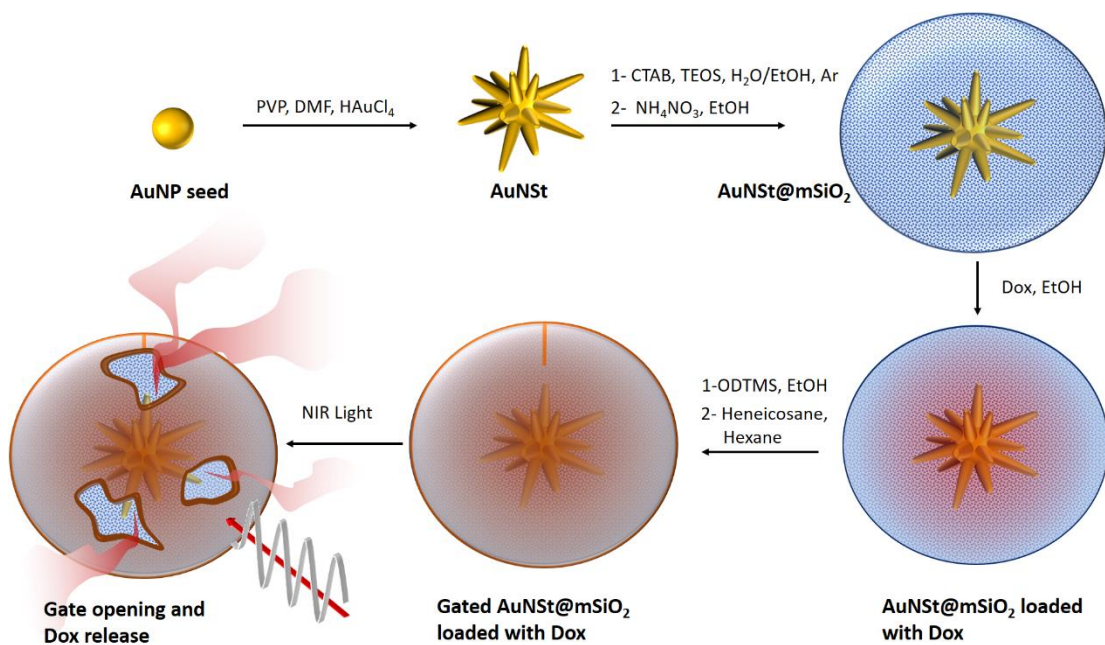


Figure 1. Representation of the drug photo-release system AuNSt@mSiO<sub>2</sub>@Dox@paraffin based on AuNSts coated with a mesoporous silica shell and paraffin as a thermo-sensitive molecular gate. The delivery of the entrapped guest (Dox) is triggered by NIR laser irradiation.

AuNSts were obtained by the seeded growth method using polyvinylpyrrolidone (PVP) solution in *N,N*-dimethylformamide (DMF). This procedure is based on the chemical reduction of AuCl<sub>4</sub><sup>-</sup> complexes by DMF, and the subsequent deposition of gold atoms in the presence of PVP on the gold nanoparticles, acting as seeds. Nanoparticle size and morphology can be tuned varying the [HAuCl<sub>4</sub>]/[seed] molar ratio and the size of the seed.<sup>36</sup> Nanostars with sizes of 120 and 250 nm were synthesized using seeds (AuNPs) of 15 and 40 nm, respectively (Figure S1). The average hydrodynamic diameters of these nanoparticles were consistent with TEM measurements (Figure 2a). The optical extinction spectra of an aqueous suspension of both sizes of AuNSts (Figure 2b) showed an absorption band/shoulder in the visible region, corresponding

to LSPR of core electrons, and another band associated with LSPR of tip electrons,<sup>43</sup> whose position varied from 835 to 1050 nm when the AuNSt size increased.

In the first step of this research, characterization of the heating ability of uncoated AuNSts (120 nm) and PVP-coated AuNSts (250 nm) was carried out quantifying both single nanoparticle and bulk heating associated with electromagnetic irradiation. Using a temperature sensitive lipid matrix, we directly assessed the plasmonic heating of single uncoated AuNSts and PVP-coated AuNSts and the thermoplasmonic associated temperature increase was measured. In the experiments, AuNSts were immobilized on a lipid bilayer with a well-known phase transition temperature incorporating fluorescent dyes with a preference for the liquid phase. The chamber was held at a temperature below the phase transition temperature, and by measuring the size of the melted area around the irradiated nanostructure (seen as the bright spots in the upper panels on Figure 2c-f), the temperature profile was quantified. More details on this technique can be found in Materials and Methods section and in Refs.<sup>15-17</sup> In the experiments, the particles were irradiated by a tightly focused NIR laser ( $\lambda=1064$  nm). The phase sensitive lipid fluorophore was FAST-DiO with a preference for the liquid state. During the experiment, the sample chamber was mounted on a temperature controller and kept at 28 °C. The phase transition temperature of the lipid bilayer was 33 °C.<sup>16</sup>

A quantitative description of the temperature increase around a particle placed in an infinite medium is under steady state conditions given by<sup>44</sup>

$$\Delta T = C \cdot I(r) \quad (1)$$

where  $C$  is a constant, including the intensity distribution at the laser focus, and physical parameters describing the nanoparticle such as its absorption cross section and the surrounding medium's thermal conductivity. The distance from the particle's center is  $r$  and Equation 1 is

valid for  $r > R$ ,  $R$  being the radius of the nanoparticle.  $P$  is the laser power.<sup>15</sup> Hence, the distance from the particle to the rim of the melted area,  $r_m$ , where the temperature is exactly the phase transition temperature,  $T(r_m) = T_m = 33$  °C, is linearly related to the power incident on the particle,  $P$ . Using image analysis,  $r_m$  was quantified and Figure 2c shows  $r_m$  as a function of laser power. Fitting Equation S1 to the data shown in Figure 2c and using the inverse relationship between  $\Delta T$  and  $r$  the entire temperature profile surrounding the irradiated particle can be quantified.

The temperature increase at the surface of the nanoparticle as a function of laser power is shown in Figure 2d. To find the temperature increase, we assumed that the average radius of the uncoated AuNSt was 60 nm (Figure 2a, S1). The error bars show one standard deviation for measurements of 10 different AuNSts. The surface temperature of uncoated AuNSt increased up to 400 °C at the applied laser powers without showing signs of deterioration of the particles.

Based on the experimental data we also inferred the absorption cross-section of gold nanostars using the following equation<sup>45</sup>

$$\sigma_{\text{abs}} = 4 \cdot \pi \cdot R \cdot \Delta T \cdot \kappa \quad (2)$$

$\Delta T$  is the increase of the nanoparticle's surface temperature,  $R$  is the radius of the AuNSt and  $\kappa$  is the heat conductivity of the combined glass and water system at 300 K which we approximate  $\kappa_{\text{glass}} = 1.1$  W m<sup>-1</sup> K<sup>-1</sup> and  $\kappa_{\text{water}} = 0.61$  W m<sup>-1</sup> K<sup>-1</sup><sup>46</sup> as suggested in reference,<sup>45</sup> and  $I$  is the  $\sigma_{\text{abs}} = 1012 \pm 145$  nm<sup>2</sup> (assuming a laser focal spot diameter of 1.95 μm).

We also measured the temperature increase of individual irradiated AuNSt with a PVP coating (Figure 2e, f). To find the temperature increase, we assumed that the average radius of a PVP-

coated AuNSt was 125 nm (Figure 2a, S1). Using Equation 2, we find absorption cross-section  $\sigma_{\text{abs}} = 13763 \pm 2588 \text{ nm}^2$ , which is 14 times larger than that of uncoated AuNSt and 2.5 times larger than that of silica-gold nanoshells (core diameter = 120 nm, shell thickness = 15 nm).<sup>17</sup> These results agree well with previous work demonstrating large energy conversion efficiency of AuNSts.<sup>10-12</sup> Above a certain laser power (~40 mW), however, the temperature does not increase with increasing laser power for the PVP-coated AuNSt. The surface temperature remains at ~120 °C + ambient temperature, hence at ~145 °C. This temperature is consistent with the melting temperature of PVP (150 °C). Hence, the flattening of the temperature curve probably indicates melting of the PVP coating. Hence, for a PVP coated AuNSt the temperature increases steeply as a function of laser power, until the surface temperature reaches the melting temperature of PVP coating. When melting is initiated, the plasmonic properties of the particle change tremendously. It is relatively normal that the plasmonic nanoparticles undergo structural changes following heating. The plasmonic nanoparticle itself reaches a steady state temperature within nano-seconds of irradiation. Moreover, the presence of a plateau (or maybe a slight decrease) in  $\Delta T$  as a function of laser power in Fig 2f indicates a continuous loss of plasmonic properties. Also, the temperature at which this happens is consistent with the known melting temperature of PVP.

These results show that by a careful choice of the irradiating electromagnetic field power, it is possible to control the particle's temperature profile. For instance, at a laser power of 30 mW the surface temperature of a PVP coated nanostar reaches 120 °C, which should be high enough to produce cargo release from the AuNSt@mSiO<sub>2</sub> nanocarrier (*vide infra*).

To analyze the heating capabilities of the nanoparticles in bulk, we irradiated aqueous suspensions of uncoated AuNSts (120 nm) with a home-made NIR laser at 808 nm,<sup>40</sup> which

match the LSPR band of the nanoparticles (Figure 2b) and measured the bulk temperature using a fiber-optic thermosensor. The temperature in nanoparticle suspensions ( $5.7 \cdot 10^9$  nanoparticles  $\text{mL}^{-1}$ ) upon 15 min of 808 nm laser irradiation at different laser power densities,  $I$ , is shown in Figure 2g. The temperature rapidly increased and reached 70 °C at laser power density of 4 W  $\text{cm}^{-2}$  and the maximum temperature in the solution decreased when lower laser power densities  $\text{cm}^{-2}$  and  $I$  was linear (Figure 2h). The absorption cross section of uncoated AuNSts can be inferred using the experimental data and the Equation 3 and 4.<sup>9</sup>

$$\rho \cdot c_p \cdot \Delta T = I \cdot A \cdot t \cdot \sigma_{\text{abs}} \cdot N \quad (3)$$

$$\sigma_{\text{abs}} = \frac{\rho \cdot c_p \cdot \Delta T}{I \cdot A \cdot t \cdot N} \quad (4)$$

$\rho$  and  $c_p$  are the specific heat capacity and the density of the suspension, respectively.  $N$  is the number of particles in the volume  $V = A \cdot l$ , where  $A$  is the area of the laser spot and  $l$  is the path length.  $\sigma_{\text{abs}} = 16000 \text{ nm}^2$ . For a comparison, in the experiments with single PVP coated AuNSts  $2588 \text{ nm}^2$ , which is comparable to the bulk value of uncoated AuNSts. These values are larger than that reported for other plasmonic gold nanoparticles, demonstrating larger energy conversion efficiency of AuNSts upon laser irradiation at LSPR wavelengths.<sup>10-12</sup>

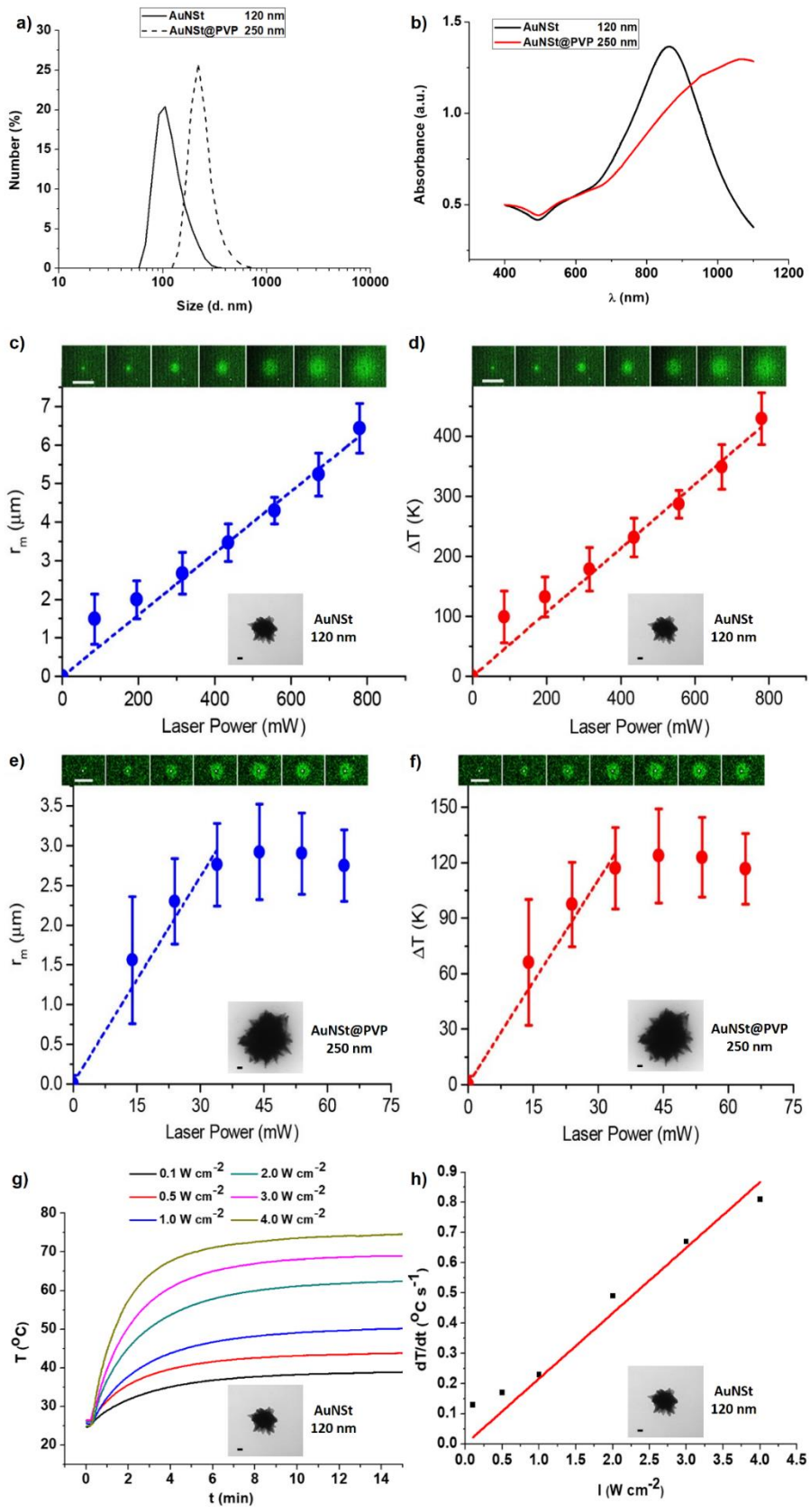


Figure 2. The hydrodynamic diameter of uncoated and PVP-coated AuNSts by DLS (a) and optical extinction spectra of both AuNSts with different diameters (b). Quantification of the surface temperature of irradiated uncoated (c, d) and PVP-coated (e, f) AuNSts. c, e) Symbols show the experimentally measured radius of the melted area around a laser irradiated AuNSt as a function of laser power at the sample. d, f) Experimentally extracted temperature increases on the surface of an irradiated AuNSt as a function of laser power. The upper panels show representative and corresponding confocal images of the melted area for laser power, the scale bar is 10  $\mu\text{m}$ . The error bars show one standard deviation, for measurements of n=10 different AuNSts and the dashed lines show a linear fit to the data. NIR laser (808 nm) induced bulk heating (g) and initial heating rate (h) of uncoated AuNSt (120 nm) suspensions at different laser power densities. Insets: TEM images of uncoated (c, d, g, h) and PVP-coated AuNSts (e, f). Scale bars: 20 nm.

After analyzing the heating ability of AuNSts, AuNSt@mSiO<sub>2</sub> nanoparticles were obtained by directly coating bare AuNSts (120 nm) with a mesoporous silica shell. The preparation protocol is based on a surfactant-templated synthesis.<sup>42</sup> The formation of the mesoporous silica shell over the AuNSts proceeds via four main steps that involve adsorption of cationic surfactant and formation of micelle assemblies on the nanoparticle's surface, hydrolysis of tetraethoxysilane (TEOS), a subsequent condensation reaction to form silica oligomers and deposition of silica oligomers on the micelle's surface and controlled silica growth. The mesoporous coating is a critical process because AuNSts can be easily reshaped due to oxidation of tip gold atoms (for instance in the presence of CTAB)<sup>47-48</sup> resulting in a decreased light absorption at 808 nm (laser wavelength), and a reduction of the light-to-heat conversion efficiency (Figure S2, S3).

In the current study several synthetic parameters, such as temperature, reaction media, base used in the preparation of the MS shell, and CTAB/TEOS molar ratio, were identified as crucial to produce AuNSt@mSiO<sub>2</sub> nanoparticles with a suitable silica shell coating (in terms of pore organization and size) while minimizing reshaping of the gold core. In the final preparation of the AuNSt@mSiO<sub>2</sub> nanoparticles: (i) the shell coating processes were carried out at 25 °C, (ii) the reaction medium was purged with argon to eliminate oxygen; (iii) a water/ethanol mixture was used as reaction medium to achieve a more controllable hydrolysis rate of the silica precursor (i.e. TEOS); (iv) ammonia was used instead of other bases; (v) the CTAB/TEOS molar ratio was adjusted in the 1.8-2.5 range and AuNSts concentration was set at ca.  $7\text{-}14\cdot 10^{-12}$  M ( $c(\text{Au})=1\text{-}2\cdot 10^{-4}$  M).

Figure 3a-d and S4 shows the obtained AuNSt@mSiO<sub>2</sub> nanoparticles following this procedure with diameters that can vary between 150-200 nm. Fine adjustments of the thickness of the silica shell can be obtained by adjusting the amount of silica precursor in the reaction mixture. The optical extinction spectrum of aqueous suspension of the AuNSt@mSiO<sub>2</sub> nanoparticles showed that the NIR LSPR band slightly shifted to higher wavelengths due to the presence of the silica shell, which changes the surface refractive index (Figure 3e).<sup>18-23</sup>

Surfactant molecules from AuNSt@mSiO<sub>2</sub> were completely removed by an ion-exchange extraction process using ammonium nitrate solution in ethanol. The removal of CTAB from the nanoparticles was monitored by FT-IR spectroscopy and zeta potential measurements (Figure S5). The characteristic peaks of CTAB at 2923, 2853 (C-H stretch) and 1478 cm<sup>-1</sup> (C-H bending) were absent in the spectrum of the AuNSt@mSiO<sub>2</sub> nanoparticles after the extraction process. The change of the zeta potential of nanoparticles from +32.5 mV to -45.3 mV also confirmed the removal of CTAB.

A detailed analysis of the nanoparticle's morphology was carried out using High Resolution Transmission Electron Microscopy (HR-TEM), Dark Field Scanning Transmission Electron Microscopy (DF-STEM) and Field Emission Scanning Electron Microscopy (FE-SEM). AuNSt@mSiO<sub>2</sub> nanoparticles contain a multi-branched gold core and a mesoporous silica shell with pores extending radially (Figure 3b-d, S6). The geometry of the mesoporous channels of the silica shell is an important parameter which may determine the efficiency of drug loading and release behavior as it affects the diffusion of the drug within the mesoporous channels. Small angle powder X-ray diffraction (PXRD) patterns of AuNSt@mSiO<sub>2</sub> nanoparticles exhibited a clear peak at  $2\theta = 2.20^\circ$ , which could be indexed to the (100) diffraction plane of a hexagonal unit cell.<sup>49</sup> This peak also suggested the presence of radial mesopore channels and an ordered mesostructure (Figure 3f). In the wide-angle PXRD pattern, four Au diffraction peaks were clearly discerned at  $2\theta = 38.16, 44.35, 64.60$  and  $77.61^\circ$ , which can be assigned to (111), (200), (220), and (311) reflections of the face-centered cubic gold lattice, respectively.<sup>50</sup> Moreover, N<sub>2</sub> adsorption-desorption isotherms of AuNSt@mSiO<sub>2</sub> nanoparticles showed a Type IV curve for mesoporous materials. The average pore size was 2.6 nm, whereas the BET surface area and total pore volume were calculated to be  $241 \text{ m}^2 \text{ g}^{-1}$  and  $0.25 \text{ cm}^3 \text{ g}^{-1}$ , respectively (Figure 3g).<sup>21-22, 24</sup>

AuNSt@mSiO<sub>2</sub> nanoparticles were loaded with the anticancer drug Dox, which can be easily detected using absorption (maximum absorption at  $\lambda = 480 \text{ nm}$ ) and fluorescence spectroscopy (maximum emission at  $\lambda = 555 \text{ nm}$ ;  $\lambda_{\text{exc}} = 488 \text{ nm}$ ). The external surface of Dox-loaded AuNSt@mSiO<sub>2</sub> was functionalized with a monolayer of octadecyltrimethoxysilane (ODTMS) and capped with a heneicosane coating. The hydrophobic ODTMS was used to facilitate the coating process of the thermosensitive paraffin layer. The paraffin coating set up a hydrophobic layer that blocked the pores and avoided leaks of the cargo (Figure 3h-k, S7, S8). Drug loading

and external surface functionalization of AuNSt@mSiO<sub>2</sub> to obtain AuNSt@mSiO<sub>2</sub>@Dox@paraffin were also optimized to prepare a hybrid nanosystem with suitable plasmonic properties. The Dox concentration in the loading solution and the loading time were adjusted to be 500 µg ml<sup>-1</sup> and 12 h, respectively, in order to obtain nanoparticles with LSPR band near to 808 nm (Figure 31).

The average hydrodynamic diameter of the nanoparticles increased from 228 to 300 nm after drug loading and paraffin coating processes, whereas the zeta potential changed from -45.3 to -17.0 mV due to the presence of Dox in the mesoporous channels and the functionalization of silanol groups at the external surface of nanoparticle with octadecyltrimethoxysilane (Figure S9). The overall fraction of organic material in the AuNSt@mSiO<sub>2</sub>@Dox@paraffin was estimated to be 25 % by TGA measurement (Figure S10), while the loaded amount of Dox was 2.4 % by spectrophotometric determination (Figure S11).

Although, the nanocomposite surface was coated with a hydrophobic layer of paraffin, the surface charge remains high enough to form stable aqueous suspensions for bioapplications. The stability of nanoparticle suspension was improved in DMEM for *in vitro* experiments with cells. The adsorption of different species (molecules and ions) onto nanoparticle surface can avoid nanoparticle flocculation and enhance suspension stability in DMEM. The nanoparticles properly interact with cells and can be internalized (*vide infra*). Moreover, the hybrid nanoparticles are stable in solid state and aqueous suspensions at room temperature. However, when nanoparticle suspension was heated at 60 °C during 48 h (for determination of Dox loading content), the silica shell was damaged, and gold core was reshaped due to hydrolysis of silica and oxidation of gold, both processes favoured at high temperatures. Furthermore, the LSPR band position shifted to lower wavelengths due to gold core reshaping (Figure S12).

Regarding the photothermal conversion efficiency of hybrid nanoparticles, Equation 4 shows that the photothermal conversion efficiency is proportional to the used laser intensity and nanomaterial's absorption cross-section. Basically, at constant laser power (intensity), the photothermal conversion efficiency of different nanomaterials can be assessed comparing their absorption cross-sections. Comparing absorbance of AuNSt@mSiO<sub>2</sub> (Figure 3e) with the absorbance of AuNSt@mSiO<sub>2</sub>@Dox@paraffin (Figure 3l) at 808 nm reveals that their absorbance, and thereby their photothermal conversion efficiency, are nearly the same. Moreover, as the absorption of Dox in water (Figure S11 b) at 808 nm is very low, the cargo could be considered as transparent at this wavelength. This explains why there is essentially no difference in the photothermal conversion efficiency for nanomaterials with or without Dox at 808 nm.

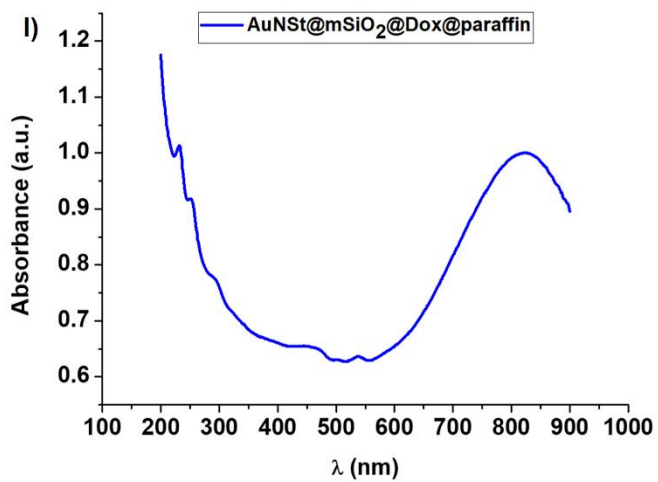
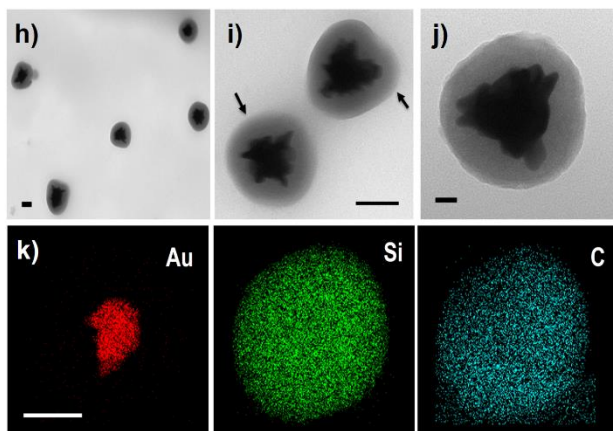
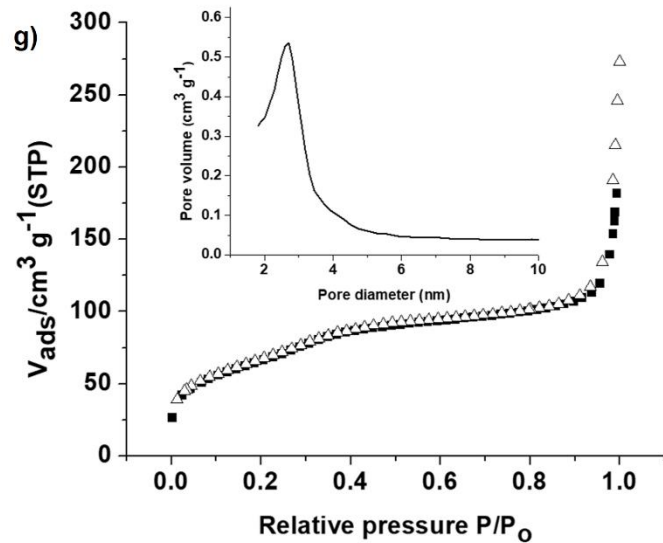
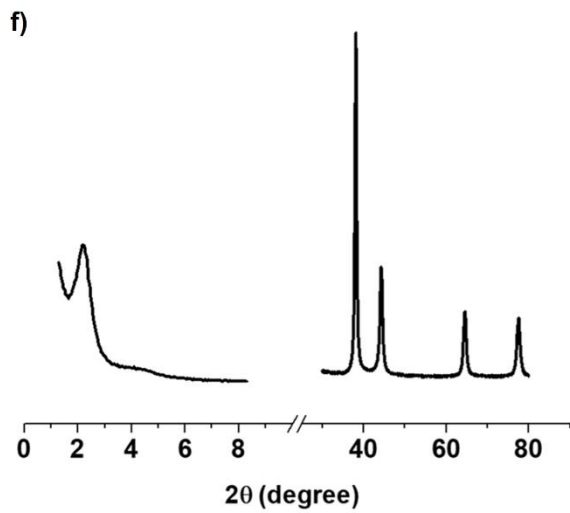
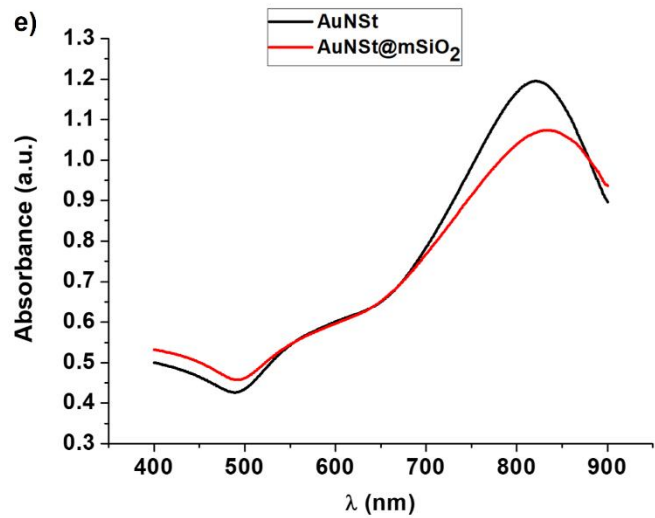
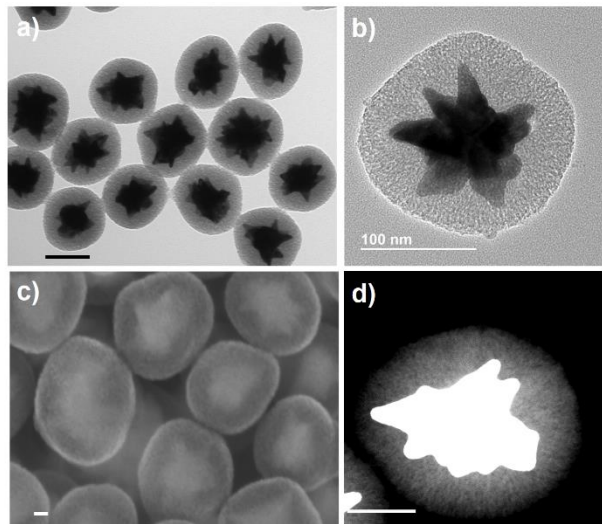


Figure 3. TEM (a), HR-TEM (b), FE-SEM (c) and DF-STEM (d) images of AuNSt@mSiO<sub>2</sub> nanoparticles. Scale bars: 100 nm (a), 50 nm (d), 20 nm (c). Optical extinction spectra (e) of AuNSt and AuNSt@mSiO<sub>2</sub> nanoparticles. PXRD patterns (f) and N<sub>2</sub> adsorption-desorption isotherms (g) of AuNSt@mSiO<sub>2</sub> nanoparticles (Inset: pore size distribution). TEM images (h, i, j) of AuNSt@mSiO<sub>2</sub>@Dox@paraffin nanoparticles and EDXS element mapping of Au, Si, and C (k); scale bars: 100 nm (h, i, k), 20 nm (j). Optical extinction spectrum of AuNSt@mSiO<sub>2</sub>@Dox@paraffin nanoparticles (l).

Aqueous suspensions of AuNSt@mSiO<sub>2</sub>@Dox@paraffin nanoparticles were irradiated using a home-made NIR laser at 808 nm,<sup>40</sup> which matches the LSPR band of the nanoparticles (Figure 3l). Cumulative release of Dox was determined using fluorescence spectroscopy. Irradiated AuNSt@mSiO<sub>2</sub>@Dox@paraffin samples showed a well-defined photo-delivery profile. Around 30 % of the total loaded drug was delivered in the first 20 min upon NIR light irradiation at power density of 4 W cm<sup>-2</sup>, whereas the non-irradiated control sample showed a negligible release, corroborating the gating efficacy of the paraffin and the photothermal conversion efficiency of the gold nanostars (Figure 4a). Using these experimental conditions, a clear heating of the water within which the nanoparticles were suspended was observed (Figure 4b). The temperature of the bulk suspension under NIR irradiation was measured to be 49 °C while the temperature of the control sample (without NIR irradiation) was 30 °C. An increase of the temperature above the paraffin melting point ( $T_m=39^{\circ}\text{C}$ ) provoked uncapping of the mesopores and dye release. These results are similar to those previously reported for drug photo-delivery systems based on plasmonic Au nanoparticles with mesoporous gated silica shell, employing Au

nanocages<sup>24</sup> and nanorods<sup>18-23</sup> as photothermal energy generators and polymers,<sup>19, 24</sup> 1-tetradecanol,<sup>18</sup> DNA,<sup>20-22</sup> and supramolecular switches<sup>23</sup> as thermo-sensible gatekeepers.

The NIR-induced heating profile and consequently the drug release can be modulated using different laser power densities (Figure 4a, b). For instance, the temperature increase ( $\Delta T$ ) of NIR laser irradiated suspensions of AuNSt@mSiO<sub>2</sub>@Dox@paraffin at 15 min was lower when irradiated by lower laser power densities (24 °C at 4 W cm<sup>-2</sup>, 17 °C at 2 W cm<sup>-2</sup>, 11 °C at 1 W cm<sup>-2</sup> and 8 °C at 0.4 W cm<sup>-2</sup>). In addition, the photothermal conversion efficiencies of hybrid nanoparticles are lower than that of AuNSts at the same mass concentration due to the fact that hybrid nanoparticles have a lower gold content. In Figures 4b and 2g we could see the NIR laser (808 nm) induced bulk heating of AuNSt@mSiO<sub>2</sub>@Dox@paraffin and AuNSt suspensions, respectively, both at 100 µg mL<sup>-1</sup>. Both the initial bulk temperature increase rate (initial slope of  $\square\square\square$ ) and the maximum temperature in the solution at the same laser power density were lower for hybrid nanoparticles. However, the photothermal conversion efficiency of hybrid nanoparticles was high enough for cancer therapy applications (hyperthermia and photothermal triggered drug delivery) (*vide infra*).

Moreover, it is possible to induce Dox release even when an aqueous suspension of the AuNSt@mSiO<sub>2</sub>@Dox@paraffin nanoparticles was irradiated at a low laser power density that produced only a slight increase of the suspension temperature. This result is consistent with a large temperature increase near the nanoparticle surface due to the high photothermal conversion efficiency of AuNSts that result in local paraffin melting and subsequent drug release. This observation agrees with the results found in the direct measurements of the local heating of AuNSt under laser irradiation (*vide ante*) in which it was found that the temperature around the AuNSt easily increases over the melting point of paraffin, even at low laser powers. This

supports the fact that Dox release from hybrid nanoparticles irradiated at low laser power density was observed, although the bulk temperature of the nanoparticle suspensions did not increase above the melting point of paraffin (Figure 2c, d, 4a, b).

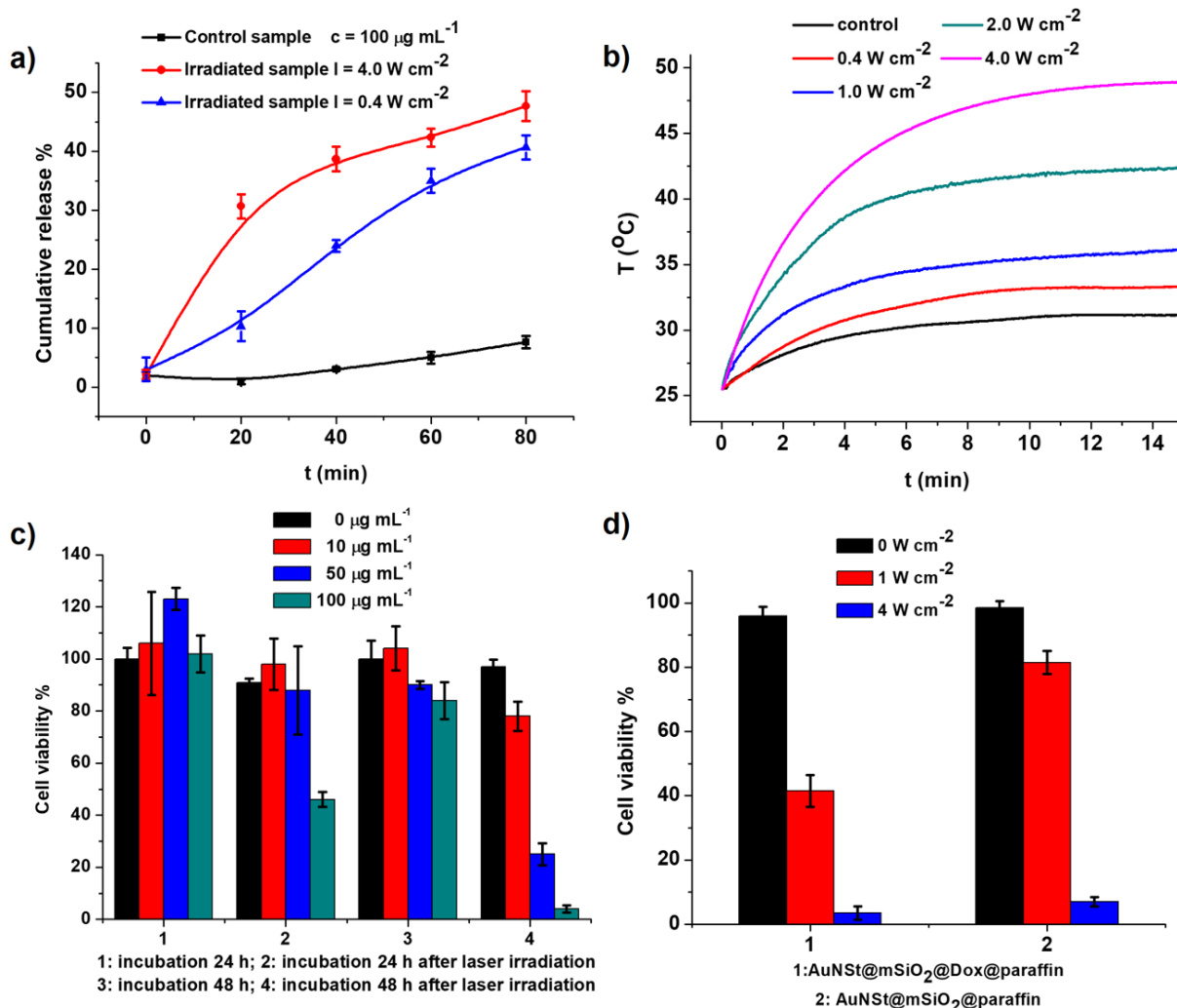


Figure 4. Cumulative release of Dox from AuNSt@mSiO<sub>2</sub>@Dox@paraffin aqueous suspensions (a) and NIR light induced heating of bulk nanoparticle suspensions (b) at different laser power densities. Cell viability of HeLa cells in the presence of AuNSt@mSiO<sub>2</sub>@Dox@paraffin nanoparticles at different concentrations and incubation times upon 808 nm laser irradiation at 4 W cm<sup>-2</sup> for 15 min (c). Cell viability of HeLa cells in the presence of

AuNSt@mSiO<sub>2</sub>@Dox@paraffin and AuNSt@mSiO<sub>2</sub>@paraffin nanoparticles upon 808 nm laser irradiation at different laser power densities for 10 min (d).

NIR light triggered drug release from AuNSt@mSiO<sub>2</sub>@Dox@paraffin nanoparticles in HeLa cells was performed to evaluate the potential application of nanoparticles in cancer therapy. The underlying idea is to design a system that could store drugs, with minimal leakage, and with the capability of releasing it upon irradiation. The therapeutic use of such system is based on the quantity of Dox released upon irradiation. In order to find the critical concentration of AuNSt@mSiO<sub>2</sub>@Dox@paraffin that can exert some therapeutic effect over cells, in a first step we decided to use the irradiation conditions that ensured the maximum drug release (Figure 4c). Once the optimal AuNSt@mSiO<sub>2</sub>@Dox@paraffin concentration was set, we then decided to study the effect of laser power (Figure 4d). Moreover, the interaction of hybrid nanoparticles with cancer cells was tested monitoring the cell internalization of nanoparticles by TEM (Figure 5). Efficient nanoparticle uptake by cells was observed after incubation of cells with nanoparticle suspension in DMEM. Cells were incubated with nanoparticles at different concentrations and then they were irradiated at 4 W cm<sup>-2</sup> for 15 min and finally incubated for 24 h or 48 h. Cell viability was determined using a WST-1 assay after the incubation period (Figure 4c). In these experiments the irradiation at 4 W cm<sup>-2</sup> did not damage the cells. As can be seen in Figure 4c, the viability of cells without nanoparticles did not decrease after laser irradiation and incubation for 24 and 48 h (black bars in groups 2 and 4). In fact, there are some reports in which higher laser power densities were employed for *in vitro* and *in vivo* photothermal therapy experiments.<sup>8</sup> Moreover, non-irradiated nanoparticles showed almost no cytotoxicity toward HeLa cells, thus demonstrating that Dox was efficiently encapsulated inside the mesoporous shell due to the

paraffin shell that prohibits leaking of the drug, even at high nanocarrier concentrations and incubation times. However, cell viability decreased when the nanoparticles were irradiated with a 808 nm laser. This effect was most remarkable at larger nanoparticle concentrations and incubation times. NIR light provoked an increase of nanoparticle's surface temperature leading to paraffin melting and Dox delivery. Larger amounts of Dox were released at higher nanocarrier concentrations and incubation times, producing consequently an enhanced cell killing effect.

To evaluate the independent effects of hyperthermia and Dox release, cells were incubated with AuNSt@mSiO<sub>2</sub>@Dox@paraffin nanoparticles or with similar nanoparticles without payload (AuNSt@mSiO<sub>2</sub>@paraffin). Cells were irradiated at different laser power densities and then incubated for 48 h. A significant difference of the cell-killing efficiency for these two types of nanoparticles upon NIR irradiation at 1 W cm<sup>-2</sup> was evidenced (Figure 4d). The viability of cells treated with AuNSt@mSiO<sub>2</sub>@paraffin (without payload) decreased to 80 % upon NIR irradiation at 1 W cm<sup>-2</sup>. NIR light induced heating of bulk AuNSt@mSiO<sub>2</sub>@Dox@paraffin nanoparticle suspensions at different laser power densities is shown in Figure 4b. The temperature in nanoparticle suspensions (100 µg mL<sup>-1</sup>) reached 36 °C (the temperature increase (ΔT) was 11 °C) upon 15 min of 808 nm laser irradiation at 1 W cm<sup>-2</sup>. Although, temperature of nanoparticle suspension did not increase above 42 °C upon irradiation, the temperature at nanoparticle surface can reach higher values inside the cells provoking the reduction of cell viability. Then, the decrease of cell viability (20%) is attributed to the effect of hyperthermia alone. Besides, a more pronounced decrease of the cell viability was observed when cells were treated with Dox loaded nanoparticles upon NIR irradiation at 1 W cm<sup>-2</sup>. This effect could be attributed to the activation of Dox released from nanoparticles, since there is essentially no

difference in the photothermal conversion efficiency for nanomaterials with or without Dox at 808 nm, thus allowing for a synergistic combination of hyperthermia and chemotherapy.

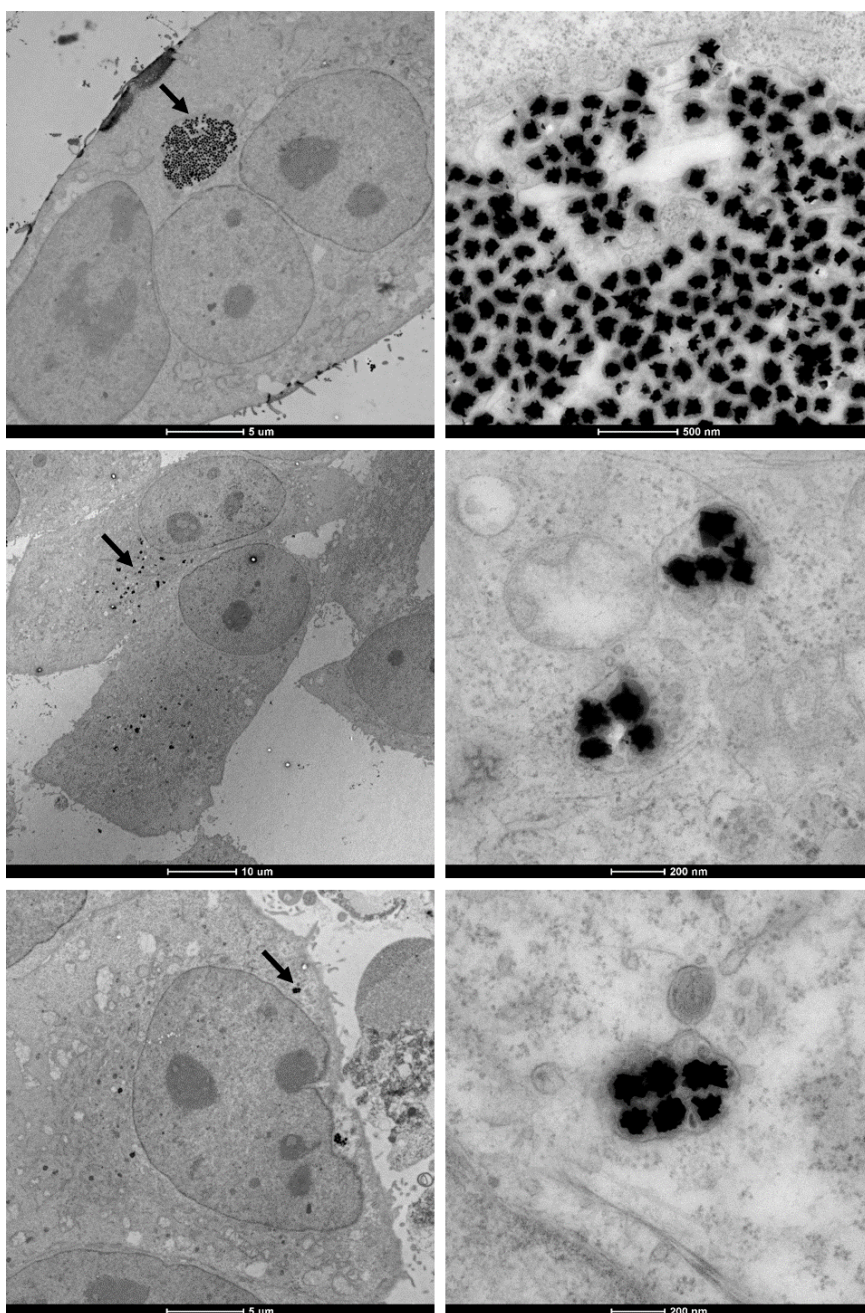


Figure 5. TEM images of HeLa cells after incubation with AuNSt@mSiO<sub>2</sub>@Dox@paraffin nanoparticles.

Also, NIR light triggered release of Dox from hybrid nanocarriers in HeLa cells was tested using confocal laser scanning microscopy (Figure 6). Cells were stained with the DNA-marker dye Hoechst 33342 and the intracellular delivery of Dox after laser irradiation was monitored by measuring the fluorescence signals of both dyes. Whereas a negligible Dox fluorescence signal can be observed in non-irradiated samples, an increase of Dox fluorescence in cells after laser irradiation was evidenced, corroborating the intracellular cargo release from nanocarrier activated by NIR light irradiation. These results show that paraffin capped AuNSt@mSiO<sub>2</sub> nanoparticles are an excellent platform for NIR light triggered drug delivery in cancer therapy applications. Moreover, the method presented allows for obtaining nanoparticles with a good quality of the silica shell while maintaining adequate and stable plasmonic properties of AuNSts for NIR triggered drug photo-release applications.

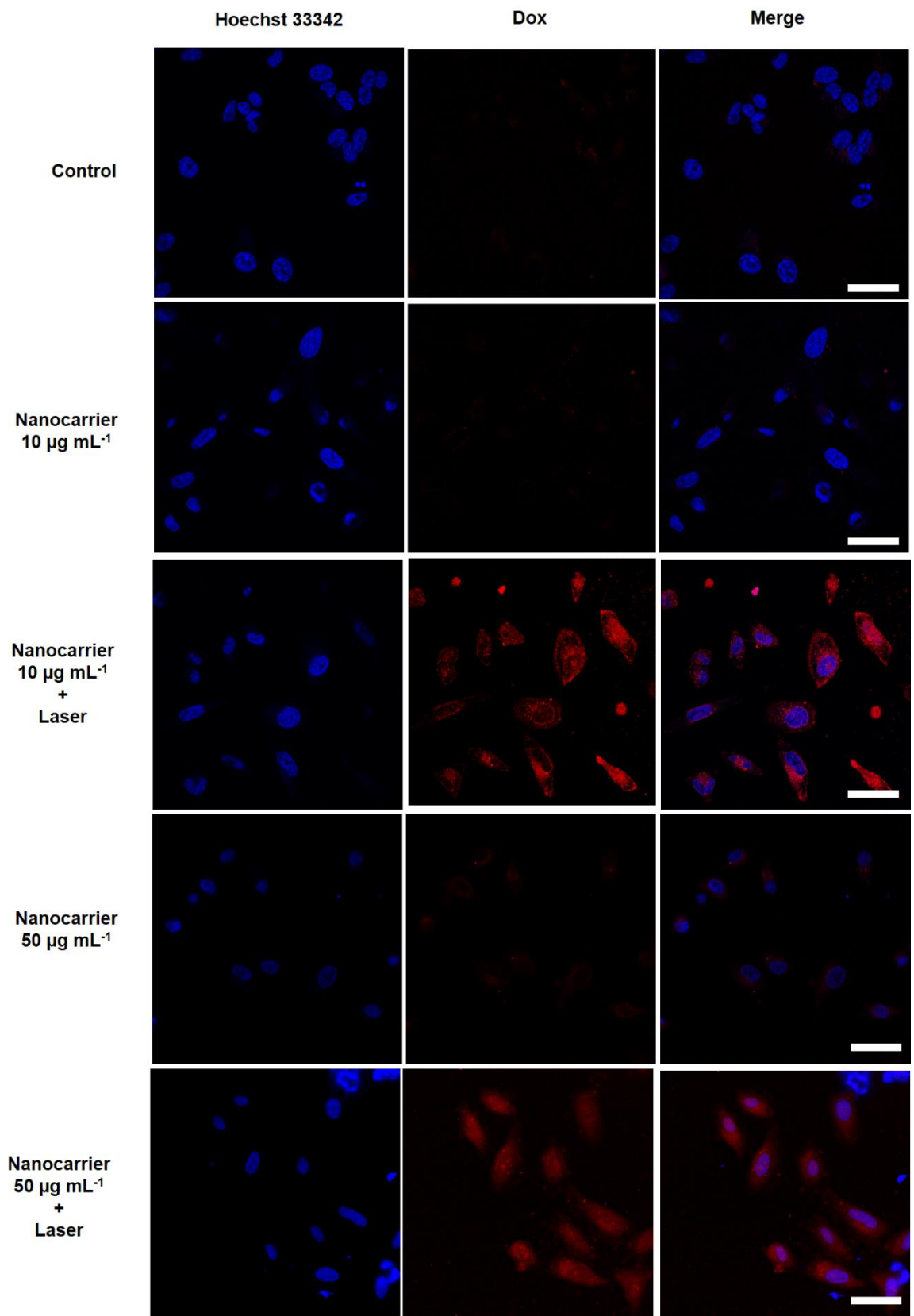


Figure 6. NIR light triggered release of Dox from AuNSt@mSiO<sub>2</sub>@Dox@paraffin nanoparticles in HeLa cells monitored by confocal laser scanning microscopy (e). From left to right: DNA marker (Hoechst 33342), Dox and combined (merge) fluorescence channels. From top to down: control cells (control), non-irradiated cells after incubation with nanoparticles at 10 µg mL<sup>-1</sup> (nanocarrier 10 µg mL<sup>-1</sup>), NIR light irradiated cells after incubation with nanoparticles at 10 µg mL<sup>-1</sup> (nanocarrier 10 µg mL<sup>-1</sup> + laser), non-irradiated cells after incubation with nanoparticles at 50 µg mL<sup>-1</sup> (nanocarrier 50 µg mL<sup>-1</sup>) and NIR light irradiated cells after incubation with nanoparticles at 50 µg mL<sup>-1</sup> (nanocarrier 50 µg mL<sup>-1</sup> + laser). Scale bars: 50 µm.

## CONCLUSIONS

In summary, we have described a novel drug photo-release system based on AuNSts coated with a mesoporous silica shell and capped with paraffin as a suitable thermo-sensitive molecular gate. The heating ability of AuNSts upon electromagnetic irradiation was quantified by irradiating single AuNSt on a temperature sensitive biological matrix. The surface temperature of uncoated AuNSts could easily reach hundreds of degrees Celsius, even at relatively low laser powers. Using larger PVP coated AuNSts caused the temperature to increase even faster with laser power, probably because the increase of nanoparticle size causes a red shift, thus displacing the LSPR peak further towards the irradiating laser wavelength. AuNSts were coated with a mesoporous silica shell using a surfactant-templated synthesis at 25 °C. Several synthetic conditions including surfactant/TEOS ratio, temperature, inert atmosphere etc., were tested in order to finally prepare AuNSt@mSiO<sub>2</sub> nanoparticles with minimum changes in the shape and absorption properties of the AuNSt core. AuNSt@mSiO<sub>2</sub> were loaded with Dox and capped with paraffin heneicosane. AuNSt@mSiO<sub>2</sub>@Dox@paraffin nanoparticles showed no leak of cargo in

aqueous solutions, whereas a significant payload delivery was observed upon NIR irradiation even at  $0.4 \text{ W cm}^{-2}$ . Dox loaded nanoparticles showed no cytotoxicity toward HeLa cells, until they were irradiated with 808 nm laser, provoking paraffin melting and drug release. We believe the method here reported for the preparation of AuNSt@mSiO<sub>2</sub>@paraffin system can be of general use for the fabrication of new drug photo-delivery systems containing AuNSts, with minimal leaks and low laser power requirements, two characteristics highly required for their implementation in enhanced chemotherapy.

#### ASSOCIATED CONTENT

**Supporting Information.** Additional TEM images, extinction spectra, FTIR spectra, EDXS, DLS and TG analysis. This material is available free of charge via the Internet at <http://pubs.acs.org>.

#### AUTHOR INFORMATION

##### **Corresponding author**

[\\*rmaez@quim.upv.es](mailto:*rmaez@quim.upv.es)

#### ACKNOWLEDGEMENT

The authors gratefully acknowledge financial support from the Spanish Government (Projects MAT2015-64139-C4-1-R and AGL2015-70235-C2-2-R), the Generalitat Valenciana (Project PROMETEOII/2014/047) and European Union (Programme European Union- Action 2-Erasmus Mundus Partnerships, GRANT AGREEMENT NUMBER - 2014 - 0870 / 001 – 001). A.S. and L.B.O. acknowledge financial support from the Novo Nordisk Foundation

(NNF14OC0011361) and from the Danish National Research Foundation (DNRF116). A. H. thanks Erasmus Mundus Programme for his PhD scholarship at EuroInkaNet project. The authors thank UPV electron microscopy and CIPF confocal and electron microscopy services for technical support.

## REFERENCES

- (1) Aznar, E.; Oroval, M.; Pascual, L.; Murguía, J. R.; Martínez-Máñez, R.; Sancenón, F. Gated Materials for on-Command Release of Guest Molecules. *Chem. Rev.* **2016**, *116*, 561–718.
- (2) Wang, D.; Liu, B.; Quan, Z.; Li, C.; Hou, Z.; Xing, B.; Lin, J. New Advances on the Marrying of Ucnps and Photothermal Agents for Imaging-Guided Diagnosis and the Therapy of Tumors. *J. Mater. Chem. B* **2017**, *5*, 2209-2230.
- (3) Liu, B.; Li, C.; Cheng, Z.; Hou, Z.; Huang, S.; Lin, J. Functional Nanomaterials for near-Infrared Triggered Cancer Therapy. *Biomater. Sci.* **2016**, *4*, 890-909.
- (4) Fan, W.; Yung, B.; Huang, P.; Chen, X. Nanotechnology for Multimodal Synergistic Cancer Therapy. *Chem. Rev.* **2017**, *117*, 13566-13638.
- (5) Zhang, L.; Chen, Y.; Li, Z.; Li, L.; Saint-Cricq, P.; Li, C.; Lin, J.; Wang, C.; Su, Z.; Zink, J. I. Tailored Synthesis of Octopus-Type Janus Nanoparticles for Synergistic Actively-Targeted and Chemo-Photothermal Therapy. *Angew. Chem. Int. Ed.* **2016**, *55*, 2118-2121.
- (6) Zhang, L.; Wang, T.; Yang, L.; Liu, C.; Wang, C.; Liu, H.; Wang, Y. A.; Su, Z. General Route to Multifunctional Uniform Yolk/Mesoporous Silica Shell Nanocapsules: A Platform for

Simultaneous Cancer-Targeted Imaging and Magnetically Guided Drug Delivery. *Chem. Eur. J.* **2012**, *18*, 12512-12521.

(7) Lim, W. Q.; Gao, Z. Plasmonic Nanoparticles in Biomedicine. *Nano Today* **2016**, *11*, 168-188.

(8) Abadeer, N. S.; Murphy, C. J. Recent Progress in Cancer Thermal Therapy Using Gold Nanoparticles. *J. Phys. Chem. C* **2016**, *120*, 4691–4716.

(9) Pino, P. d.; Pelaz, B. Hyperthermia Using Inorganic Nanoparticles. In *Frontiers of Nanoscience*; Fuente, J. M. d. l., Grazu, V., Eds.; Elsevier Ltd: Oxford, 2012; pp 309-335.

(10) Jaque, D.; Maestro, L. M.; Rosal, B. d.; Haro-Gonzalez, P.; Benayas, A.; Plaza, J. L.; Rodríguez, E. M.; Solé, J. G. Nanoparticles for Photothermal Therapies. *Nanoscale* **2014**, *6*, 9494-9530.

(11) Maestro, L. M.; Haro-González, P.; Sánchez-Iglesias, A.; Liz-Marzán, L. M.; Solé, J. G.; Jaque, D. Quantum Dot Thermometry Evaluation of Geometry Dependent Heating Efficiency in Gold Nanoparticles. *Langmuir* **2014**, *30*, 1650–1658.

(12) Wang, Y.; Black, K. C. L.; Luehmann, H.; Li, W.; Zhang, Y.; Cai, X.; Wan, D.; Liu, S.-Y.; Li, M.; Kim, P.; Li, Z.-Y.; Wang, L. V.; Liu, Y.; Xia, Y. Comparison Study of Gold Nanohexapods, Nanorods, and Nanocages for Photothermal Cancer Treatment. *ACS Nano* **2013**, *7*, 2068–2077.

(13) Trigari, S.; Rindi, A.; Margheri, G.; Sottini, S.; Dellepiane, G.; Giorgetti, E. Synthesis and Modelling of Gold Nanostars with Tunable Morphology and Extinction Spectrum. *J. Mater. Chem.* **2011**, *21*, 6531-6540.

- (14) Rodríguez-Oliveros, R.; Sánchez-Gil, J. A. Gold Nanostars as Thermoplasmonic Nanoparticles for Optical Heating. *Optics Express* **2012**, *20*, 621-626.
- (15) Bendix, P. M.; Reihani, S. N. S.; Oddershede, L. B. Direct Measurements of Heating by Electromagnetically Trapped Gold Nanoparticles on Supported Lipid Bilayers. *ACS Nano* **2010**, *4*, 2256–2262.
- (16) Ma, H.; Tian, P.; Pello, J.; Bendix, P. M.; Oddershede, L. B. Heat Generation by Irradiated Complex Composite Nanostructures. *Nano Lett.* **2014**, *14*, 612–619.
- (17) Jørgensen, J. T.; Norregaard, K.; Tian, P.; Bendix, P. M.; Kjaer, A.; Oddershede, L. B. Single Particle and Pet-Based Platform for Identifying Optimal Plasmonic Nano-Heaters for Photothermal Cancer Therapy. *Sci. Rep.* **2016**, *6*, 30076-30086.
- (18) Liu, J.; Detrembleur, C.; Pauw-Gillet, M.-C. D.; Mornet, S.; Jérôme, C.; Duguet, E. Gold Nanorods Coated with Mesoporous Silica Shell as Drug Delivery System for Remote near Infrared Light-Activated Release and Potential Phototherapy. *Small* **2015**, *11*, 2323–2332.
- (19) Tang, H.; Shen, S.; Guo, J.; Chang, B.; Jiang, X.; Yang, W. Gold Nanorods@Msio2 with a Smart Polymer Shell Responsive to Heat/near-Infrared Light for Chemo-Photothermal Therapy. *J. Mater. Chem.* **2012**, *22*, 16095-16103.
- (20) Chang, Y.-T.; Liao, P.-Y.; Sheu, H.-S.; Tseng, Y.-J.; Cheng, F.-Y.; Yeh, C.-S. Near-Infrared Light-Responsive Intracellular Drug and Sirna Release Using Au Nanoensembles with Oligonucleotide-Capped Silica Shell. *Adv. Mater.* **2012**, *24*, 3309–3314.

(21) Yang, X.; Liu, X.; Liu, Z.; Pu, F.; Ren, J.; Qu, X. Near-Infrared Light-Triggered, Targeted Drug Delivery to Cancer Cells by Aptamer Gated Nanovehicles. *Adv. Mater.* **2012**, *24*, 2890–2895.

(22) Li, N.; Yu, Z.; Pan, W.; Han, Y.; Zhang, T.; Tang, B. A near-Infrared Light-Triggered Nanocarrier with Reversible DNA Valves for Intracellular Controlled Release. *Adv. Funct. Mater.* **2013**, *23*, 2255–2262.

(23) Li, H.; Tan, L.-L.; Jia, P.; Li, Q.-L.; Sun, Y.-L.; Zhang, J.; Ning, Y.-Q.; Yu, J.; Yang, Y.-W. Near-Infrared Light-Responsive Supramolecular Nanovalve Based on Mesoporous Silica-Coated Gold Nanorods. *Chem. Sci.* **2014**, *5*, 2804-2808.

(24) Yang, J.; Shen, D.; Zhou, L.; Li, W.; Li, X.; Yao, C.; Wang, R.; El-Toni, A. M.; Zhang, F.; Zhao, D. Spatially Confined Fabrication of Core–Shell Gold Nanocages@Mesoporous Silica for near-Infrared Controlled Photothermal Drug Release. *Chem. Mater.* **2013**, *25*, 3030–3037.

(25) Liu, Y.; Yuan, H.; Kersey, F. R.; Register, J. K.; Parrott, M. C.; Vo-Dinh, T. Plasmonic Gold Nanostars for Multi-Modality Sensing and Diagnostics. *Sensors* **2015**, *15*, 3706-3720.

(26) Yuan, H.; Gomez, J. A.; Chien, J. S.; Zhang, L.; Wilson, C. M.; Li, S.; Fales, A. M.; Liu, Y.; Grant, G. A.; Mirotsoy, M.; Dzau, V. J.; Vo-Dinh, T. Tracking Mesenchymal Stromal Cells Using an Ultra-Bright Tat-Functionalized Plasmonic-Active Nanoplatfom. *J. Biophotonics* **2016**, *9*, 406–413.

(27) Liu, Y.; Yuan, H.; Fales, A. M.; Register, J. K.; Vo-Dinh, T. Multifunctional Gold Nanostars for Molecular Imaging and Cancer Therapy. *Frontiers in Chemistry* **2015**, *3*, 1-7.

- (28) Espinosa, A.; Silva, A. K. A.; Sánchez-Iglesias, A.; Grzelczak, M.; Péchoux, C.; Desboeufs, K.; Liz-Marzán, L. M.; Wilhelm, C. Cancer Cell Internalization of Gold Nanostars Impacts Their Photothermal Efficiency in Vitro and in Vivo: Toward a Plasmonic Thermal Fingerprint in Tumoral Environment. *Adv. Healthcare Mater.* **2016**, *5*, 1040–1048.
- (29) Turkevich, J.; Stevenson, P. C.; Hillier, J. A Study of the Nucleation and Growth Processes in the Synthesis of Colloidal Gold. *Discuss. Faraday Soc.* **1951**, *11*, 55-75.
- (30) Enustun, B. V.; Turkevich, J. Coagulation of Colloidal Gold. *J. Am. Chem. Soc.* **1963**, *85*, 3317-3328.
- (31) Frens, G. Controlled Nucleation for the Regulation of the Particle Size in Monodisperse Gold Suspensions *Nature Physical Science* **1973**, *241*, 20-22.
- (32) Bastús, N. G.; Comenge, J.; Puntès, V. Kinetically Controlled Seeded Growth Synthesis of Citrate-Stabilized Gold Nanoparticles of up to 200 Nm: Size Focusing Versus Ostwald Ripening. *Langmuir* **2011**, *27*, 11098–11105.
- (33) Graf, C.; Vossen, D. L. J.; Imhof, A.; Blaaderen, A. v. A General Method to Coat Colloidal Particles with Silica. *Langmuir* **2003**, *19*, 6693-6700.
- (34) Scarabelli, L.; Grzelczak, M.; Liz-Marzán, L. M. Tuning Gold Nanorod Synthesis through Pre-Reduction with Salicylic Acid. *Chem. Mater.* **2013**, *25*, 4232–4238.
- (35) Hendel, T.; Wuithschick, M.; Kettemann, F.; Birnbaum, A.; Rademann, K.; Polte, J. r. In Situ Determination of Colloidal Gold Concentrations with Uv–Vis Spectroscopy: Limitations and Perspectives. *Anal. Chem.* **2014**, *86*, 11115-11124.

- (36) Barbosa, S.; Agrawal, A.; Rodríguez-Lorenzo, L.; Pastoriza-Santos, I.; Alvarez-Puebla, R. A.; Kornowski, A.; Weller, H.; Liz-Marzán, L. M. Tuning Size and Sensing Properties in Colloidal Gold Nanostars. *Langmuir* **2010**, *26*, 14943–14950.
- (37) Kumar, P. S.; Pastoriza-Santos, I.; Rodríguez-González, B.; Abajo, F. J. G. d.; Liz-Marzán, L. M. High-Yield Synthesis and Optical Response of Gold Nanostars. *Nanotechnology* **2008**, *19*, 015606-015612.
- (38) Khoury, C. G.; Vo-Dinh, T. Gold Nanostars for Surface-Enhanced Raman Scattering: Synthesis, Characterization and Optimization. *J. Phys. Chem. C* **2008**, *112*, 18849–18859.
- (39) Aznar, E.; Mondragón, L.; Ros-Lis, J. V.; Sancenón, F.; Marcos, M. D.; Martínez-Máñez, R.; Soto, J.; Pérez-Payá, E.; Amorós, P. Finely Tuned Temperature-Controlled Cargo Release Using Paraffin-Capped Mesoporous Silica Nanoparticles. *Angew. Chem.* **2011**, *123*, 11368 – 11371.
- (40) Montes-Robles, R.; Hernández, A.; Ibáñez, J.; Masot-Peris, R.; Torre, C. d. I.; Martínez-Máñez, R.; García-Breijo, E.; Fraile, R. Design of a Low-Cost Equipment for Optical Hyperthermia. *Sensors and Actuators A* **2017**, *255*, 61–70.
- (41) Kedia, A.; Kumar, P. S. Controlled Reshaping and Plasmon Tuning Mechanism of Gold Nanostars. *J. Mater. Chem. C* **2013**, *1*, 4540-4549.
- (42) Sanz-Ortiz, M. N.; Sentosun, K.; Bals, S.; Liz-Marzán, L. M. Templated Growth of Surface Enhanced Raman Scattering-Active Branched Gold Nanoparticles within Radial Mesoporous Silica Shells. *ACS Nano* **2015**, *9*, 10489-10497.

- (43) Guerrero-Martínez, A.; Barbosa, S.; Pastoriza-Santos, I.; Liz-Marzán, L. M. Nanostars Shine Bright for You: Colloidal Synthesis, Properties and Applications of Branched Metallic Nanoparticles. *Current Opinion in Colloid & Interface Science* **2011**, *16*, 118–127.
- (44) Goldenberg, H.; Tranier, C. J. Heat Flow in an Infinite Medium Heated by a Sphere. *J. Appl. Phys.* **1952**, *3*, 296-298.
- (45) Baffou, G.; Berto, P.; Ureña, E. B.; Quidant, R.; Monneret, S.; Polleux, J.; Rigneault, H. Photoinduced Heating of Nanoparticle Arrays. *ACS Nano* **2013**, *7*, 6478–6488.
- (46) Powell, R. W.; Ho, C. Y.; Liley, P. E. Thermal Conductivity of Selected Materials. *National Standard Reference Data Series- National Bureau of Standards* **1966**.
- (47) Rodríguez-Fernández, J.; Pérez-Juste, J.; Mulvaney, P.; Liz-Marzán, L. M. Spatially-Directed Oxidation of Gold Nanoparticles by Au(III)-Ctab Complexes. *J. Phys. Chem. B* **2005**, *109*, 14257-14261.
- (48) Zheng, Y.; Zeng, J.; Ruditskiy, A.; Liu, M.; Xia, Y. Oxidative Etching and Its Role in Manipulating the Nucleation and Growth of Noble-Metal Nanocrystals. *Chem. Mater.* **2014**, *26*, 22–33.
- (49) Nooney, R. I.; Thirunavukkarasu, D.; Chen, Y.; Josephs, R.; Ostafin, A. E. Self-Assembly of Mesoporous Nanoscale Silica/Gold Composites. *Langmuir* **2003**, *19*, 7628-7637.
- (50) Liu, W.; Zhu, Z.; Deng, K.; Li, Z.; Zhou, Y.; Qiu, H.; Gao, Y.; Che, S.; Tang, Z. Gold Nanorod@Chiral Mesoporous Silica Core–Shell Nanoparticles with Unique Optical Properties. *J. Am. Chem. Soc.* **2013**, *135*, 9659–9664.